(This is a sample cover image for this issue. The actual cover is not yet available at this time.)

JOURNAL OF THE MECHANICAL BEHAVIOR OF BIOMEDICAL MATERIALS 15 (2012) 78–92

Available online at www.sciencedirect.com

SciVerse ScienceDirect

journal homepage: www.elsevier.com/locate/jmbbm

Research Paper

Fatigue life assessment of cardiovascular balloon-expandable stents: A two-scale plasticity–damage model approach

H.A.F. Argente dos Santos[a,*], F. Auricchio[b,c,d], M. Conti[b]

[a]Department of Civil Engineering and Architecture, Instituto Superior Técnico, Av. Rovisco Pais, 1049-001 Lisboa Codex, Portugal
[b]Dipartimento di Ingegneria Civile ed Architettura, Università degli studi di Pavia, Italy
[c]IMATI-CNR, Pavia, Italy
[d]EUCENTRE, Via Ferrata 1, I-27100 Pavia, Italy

ARTICLE INFO

Article history:
Received 13 June 2012
Accepted 19 June 2012
Available online 27 June 2012

Keywords:
Cardiovascular balloon-expandable stents
Fatigue life assessment
Continuum damage mechanics
Two-scale plasticity–damage model

ABSTRACT

Cardiovascular disease has become a major global health care problem in the present decade. To tackle this problem, the use of cardiovascular stents has been considered a promising and effective approach. Numerical simulations to evaluate the *in vivo* behavior of stents are becoming more and more important to assess potential failures. As the material failure of a stent device has been often associated with fatigue issues, as a result of the high number of cyclic loads these devices are subjected to *in vivo*, numerical approaches for fatigue life assessment of stents has gained special interest in the engineering community. Numerical fatigue predictions can be used to modify the design and prevent failure, without making and testing numerous physical devices, thus preventing from undesired fatigue failures. This work presents a fatigue life numerical method for the analysis of cardiovascular balloon-expandable stainless steel stents. The method is based on a two-scale continuum damage mechanics model in which both plasticity and damage mechanisms are assumed to take place at a scale smaller than the scale of the representative volume element. The fatigue failure criterion is based on the Soderberg relation. The method is applied to the fatigue life assessment of both *PalmazShatz* and *Cypher* stent designs. Validation of the method is performed through comparison of the obtained numerical results with some experimental results available for the *PalmazShatz* stent design. The present study gives also possible directions for future research developments in the framework of the numerical fatigue life assessment of real balloon-expandable stents.

1. Introduction

Stents are small tube-like medical devices used to restore patency of blood vessels where the lumen area is reduced due to atherosclerosis, a degenerative disease of the vessel wall. The stent acts as a mechanical scaffold for the vessel and its implant is performed by a minimally invasive procedure inserting a catheter through a small incision in the femoral artery.

*Corresponding author.
E-mail address: hugofreixialsantos@gmail.com (H.A.F. Argente dos Santos).

1751-6161/$ - see front matter © 2012 Elsevier Ltd. All rights reserved.
http://dx.doi.org/10.1016/j.jmbbm.2012.06.011

Stenting is nowadays a common clinical practice especially for the treatment of coronary stenosis, which has a high economical and social impact in the Western countries (AHA, 2010). The majority of coronary stents are manufactured laser-cutting the stent pattern from a thin tube of medical grade 316L austenitic stainless steel. After annealing and electro-polishing treatments, the stent is mounted on an angioplasty balloon. The balloon expansion drives the stent expansion leading to plastic deformation providing a permanently expanded state. Clearly, a certain level of elastic recoil occurs on deflation and removal of the balloon (Aziz et al., 2007).

As the heart beats, and hence the arteries pulse, at typically 70 times per minute (around 40 million times per year), stents are subjected to long-term cyclic loading conditions.

The US regulatory authority over these devices (FDA) recommends that stents must withstand 10–15 years of pulsatile loading *in vivo*, the equivalent to 400–600 million loading cycles. Therefore, the long-term structural integrity of a stent, in particular its mechanical fatigue behavior, must be one of the major design considerations.

The fatigue behavior of a stent results from a complex interaction of two stress states. The first of these is the state to which the device is statically loaded and deformed as a result from the positioning of the stent within the vessel. This state is typically characterized by high plastic strain levels in some parts of the stent and, therefore, by high residual stresses. A second state is then imposed, which corresponds to the cyclic (alternating) component of the loading as a consequence of the pulsatile blood-pressure variations in the vessel. The first state will be hereafter termed the mean stress state, whereas the second will be referred to as the alternating stress state.

For stents made of standard metallic materials, the fatigue damage induced by the alternating stress state can be divided into three main stages: crack initiation, stable crack growth and final failure (Suresh, 1998; Schijve, 2009). Approaches to fatigue life prediction traditionally focus on one of the two first stages of the fatigue damage process. Total-life approaches, often also referred to as safe-life approaches, define failure as the initiation of a crack and, accordingly, the number of loading cycles before crack initiation is assumed as the total fatigue life. These approaches are based either on $S-N$ or $\varepsilon-N$ experiments, both giving the number of loading cycles N until a plain specimen fails (fatigue life), the former considering the specimen under constant cyclic stress amplitude (with zero mean stress), whereas the latter considering the specimen under a constant strain amplitude. While $S-N$ curves are suited for materials in the high-cycle fatigue regime, *i.e.*, where typically more than 10^5 cycles at low stresses are required to failure and where deformation is primarily elastic, $\varepsilon-N$ curves are employed typically for materials in the low-cycle regime, *i.e.*, where less than 10^5 cycles characterized by stresses that are high enough for plastic deformations to occur are required to failure. Damage-tolerant approaches, on the other hand, define life in terms of time or number of loading cycles to propagate the largest pre-existing flaw to catastrophic failure, typically resorting to linear elastic fracture mechanics tools.

Stents are typically designed to work in the so-called high-cycle fatigue regime. Under this regime, the equivalent von Mises stresses are above the fatigue limit (usually defined as the stress amplitude requiring 10^6 load cycles up to rupture), but considerably below the yield stress (Suresh, 1998). This leads very often to a number of loading cycles to failure greater than 10^5. In this regime damage can be considered as a microscale process of progressive deterioration of the material with no influence on the mesoscopic behavior where, up to crack initiation, the material deforms primarily elastically at the scale of the representative volume element (mesoscale), and coupling between plasticity and damage may be neglected everywhere but at the microscale (Lemaitre and Desmorat, 2005).

Crack initiation modeling using the classical linear elastic fracture mechanics theory is difficult in the high-cycle fatigue regime, since the scale where the mechanisms operate is not the mesoscale. In fact, although the linear elastic fracture mechanics theory has proved its capability to reflect the main trends of crack propagation or the advanced part of damage, when dealing with small cracks (microcracks), fracture mechanics tools are inadequate. For stents, this inadequacy was confirmed by (James and Sire, 2010).

The material behavior in the high-cycle fatigue regime may be well characterized by resorting to the continuum damage mechanics theory, first introduced by (Kachanov, 1958) and (Rabotnov, 1969). This theory, based on irreversible thermodynamics, has been widely applied to study the behavior of rocks and concrete as well as ductile fracture, creep rupture and fatigue failure of metals. The material degradation caused by the initiation, growth and coalescence of microcracks in a material element due to cyclic loading is well suited for characterization by the theory of continuum damage mechanics, *e.g.* (Chaboche, 1988a, 1988b; Lemaitre and Chaboche, 1990; Lemaitre, 1992). Centered on microcrack development, the continuum damage mechanics theory provides a good understanding of the mechanisms of fatigue failure by means of damage variables, taken as internal variables within the framework of the thermodynamics of irreversible processes, which represent the deterioration of a material element. Different continuum damage mechanics based models have been proposed in the literature for the high-cycle fatigue analysis of metallic structures. Among others, models based on two-scale approaches in which micro and mesoscales are linked by means of a localization law (Lemaitre and Doghri, 1994; Lemaitre et al., 1999; Desmorat and Lemaitre, 2001; Lemaitre and Desmorat, 2005; Desmorat, 2006; Desmorat et al., 2007; Flaceliere et al., 2007a, 2007b), and models relying on a single macroscopic (engineering) scale (Oller et al., 2005; Ottosen et al., 2008) can be found in the fatigue of metals literature. However, due to its inherent multi-scale manifestation, the high-cycle fatigue damage can only be properly captured by resorting to models which are capable of dealing with plasticity and damage on a scale smaller than the macroscopic scale, as for instance the two-scale models cited above.

Furthermore, as the experiments for such small devices are challenging, see *e.g.* (Weiss et al., 2009), the assessment of fatigue life of a coronary stent is not a trivial task. Computational tools, as finite element analysis, have already proved extensively their usefulness to analyze both the design of the coronary stents and their interaction with the vessel wall, see *e.g.* the works by (Auricchio et al., 2001; Migliavacca et al.,

2002; Lally et al., 2005; Wang et al., 2006; De Beule et al., 2008; Ju et al., 2008; Mortier et al., 2010). None of these works have however addressed the fatigue life assessment of stents. In fact, only a few works dealing with the numerical assessment of the fatigue life of stents can be found in the literature, see *e.g.* the works by (Perry et al., 2002; Marrey et al., 2006; Pelton et al., 2008; Li et al., 2010; Arakere et al., 2012). In particular, Marrey et al. (2006) introduced a damage-tolerant approach for the analysis of cardiovascular stents, where the design life is evaluated using a fracture mechanics methodology. The approach can be used to quantify the effect of flaws in terms of their potential effect on device failure. Li et al. (2010) proposed a new methodology based on both computational and experimental techniques to analyze the stress distribution of different phases and evaluate the fatigue life according to Goodman (1899) criteria. The obtained results indicate that the maximum and alternating stresses were always located at the curvature areas of the rings. The common drawback of these methodologies is the use of continuum-based material models, which are incapable of explicitly capturing microstructural effects. Furthermore, as underlined by Wiersma et al. (2006), data from conventional macroscopic specimens cannot be used to realistically predict the behavior of microscopic components, like stent struts, with a size comparable to the characteristic scale of its microstructure, *e.g.*, the grain size. In these situations, continuum approaches relying on macroscopic material properties to model material behavior may be regarded as somewhat questionable, and alternative numerical analyses, based on crystal plasticity, providing a means of explicitly modeling microstructural grains in a polycrystalline material, may be needed (Savage et al., 2004; You et al., 2006; Harewood and McHugh, 2007; McGarry et al., 2004, 2007). This methodology requires, however, an accurate representation of the microstructure, based on high-resolution measures and images.

It is the purpose of this work to present a numerical fatigue life approach for the analysis of cardiovascular balloon-expandable (stainless steel) stents that can provide useful information either to be used for product improvement or for clinicians to make life-saving decisions. This approach incorporates the two-scale plasticity–damage model proposed by (Lemaitre et al., 1999; Desmorat and Lemaitre, 2001), modified by means of the so-called Soderberg (1939) fatigue relation in order to take into account the high mean stress effects inherent to cardiovascular stents.

The outline of the paper is as follows: the thermodynamics framework of the two-scale plasticity–damage model of Lemaitre, along with its corresponding plasticity and damage evolution laws, damage and microcrack initiation criteria and numerical implementation scheme are introduced in Section 2. The application of this model to the fatigue life prediction of two different cardiovascular balloon-expandable stainless steel stent designs is considered in Section 3, which has in turn been subdivided into two main parts: the first part presents the finite element analysis set-up, resembling both stent deployment within the cardiovascular artery and the subsequently pulsatile loading, whereas the second part addresses the fatigue life assessment methodology, in particular, the material parameters identification issue, the Soderberg fatigue limit criterion, and the application of the method to the analysis of the two stent designs under investigation. Some directions for the improvement of the proposed numerical fatigue life approach are indicated in Section 4 and, finally, the conclusions are given in Section 5.

We use the following notation. Bold face lower-case letters are used to denote vectors, and bold face upper-case letters to denote matrices. The components of vectors and matrices are denoted by light-face letters, as well as the ordinary scalars. Finally, we define the double dot product of two tensors using a double dot: *e.g.*, $\mathbf{A} : \mathbf{B} = c$, with A and B two tensors and c a real scalar.

2. The two-scale plasticity–damage model of Lemaitre

Several typical material failure problems have been successfully modeled by resorting to the continuum damage mechanics theory. Its suitability to capture both crack initiation and crack propagation under arbitrary loading conditions makes it one of the most important tools for material failure modeling. Damage mechanics models require accurate material constitutive equations and damage evolution equations obtained from precise phenomenological (mesoscale) descriptions of the material behavior.

However, in the high-cycle fatigue regime, mesoscopic plasticity is, for the most part, negligible, and crack initiation occurs in localized plasticity spots surrounded by a material in the elastic range. Hence, damage is localized on a microscopic scale with negligible influence on the mesoscopic scale. In other words, the coupling between damage and plasticity may be neglected everywhere in the structure except in the microscale where the damage develops.

One of the first attempts presented in the literature to extend the framework of continuum damage mechanics to the fatigue field including its multi-scale aspect is the model proposed by Lemaitre (1985), further extended and improved in Lemaitre and Doghri (1994), Lemaitre et al. (1999), Desmorat and Lemaitre (2001), and Lemaitre and Desmorat (2005). This model considers two phases, see Fig. 1. One represents a microscopic spherical inclusion with an elasto-plastic coupled with isotropic damage behavior, and the other represents a mesoscopic elastic (possibly elasto-plastic) matrix, represented through the representative volume element (RVE), in which the inclusion is embedded. The microscale variables are denoted with a superscript μ. The two phases are assumed to have the same elastic behavior, characterized by Young's modulus E and Poisson's coefficient ν. In addition, the matrix behavior is characterized by its yield stress σ_y, its ultimate stress σ_u and its asymptotic fatigue limit σ_f, obviously lower than σ_y, viewed as the asymptote of a $S-N$ curve. As for the inclusion, different elasto-plastic material behaviors have been considered. In Lemaitre (1985), the behavior of the inclusion was assumed as elasto-plastic perfect coupled with damage. The extension to stepwise perfect plasticity was considered in Lemaitre and Doghri (1994). Further extensions were given by Lemaitre et al. (1999) and Lemaitre and Desmorat (2005), who proposed a new model incorporating also strain hardening effects. According to Lemaitre et al. (1999) and Lemaitre and Desmorat (2005), this new model produces results which are coherent with most of the experimental

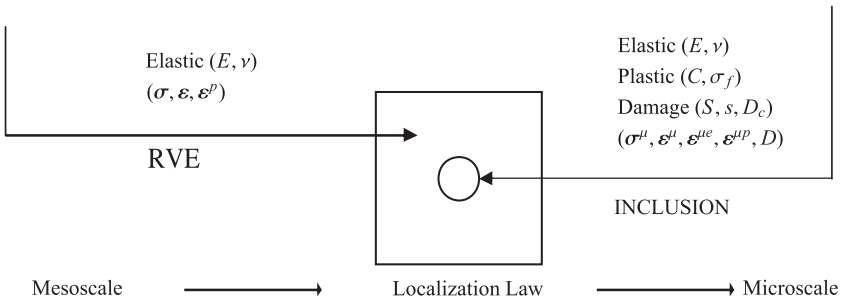

Fig. 1 – Two-scale damage model.

results obtained in the high-cycle fatigue regime of metals, namely, results which are not dependent on the mean shear stresses, results which capture the nonlinear damage accumulation effect and also results which reflect the beneficial effect of some non-proportional loadings. A weakness of the inclusion is considered by assuming that its corresponding yield stress is identical to the asymptotic fatigue limit of the matrix material, *i.e.*, $\sigma_y^\mu = \sigma_f$. Note that, on the basis of this assumption, neither plasticity nor damage can develop and, therefore, no fatigue cracks can initiate below the fatigue limit.

2.1. *Thermodynamics framework*

The model is developed assuming the existence of a free energy $\rho\phi^\mu$. Damage is represented by an internal scalar variable D, assumed to range between 0 and a critical material parameter corresponding to microcrack initiation, D_c, with $D_c \leq 1$. Note that, as damage is only considered at the microscale, the superscript μ has been omitted from the microscopic damage variable D. The coupling between elasticity and damage at the microscale is considered within the framework of the thermodynamics of (isothermal) irreversible processes by means of the effective stress concept first proposed by Kachanov (1958). Hence, microscopic actual stresses $\boldsymbol{\sigma}^\mu$ and microscopic effective stresses $\tilde{\boldsymbol{\sigma}}^\mu$ are assumed to obey the following relation:

$$\tilde{\boldsymbol{\sigma}}^\mu = \frac{\boldsymbol{\sigma}^\mu}{(1-D)}$$

The microscopic total strain is assumed to be partitioned into elastic and plastic parts as follows:

$$\boldsymbol{\varepsilon}^\mu = \boldsymbol{\varepsilon}^{\mu e} + \boldsymbol{\varepsilon}^{\mu p}$$

The free energy is taken as the sum of an elastic energy and a plastic energy as follows:

$$\rho\phi^\mu = \rho\phi_e^\mu + \rho\phi_p^\mu$$

with ρ the mass density of the material. The elastic energy is considered as

$$\rho\phi_e^\mu(\boldsymbol{\varepsilon}^\mu - \boldsymbol{\varepsilon}^{\mu p}, D) = \tfrac{1}{2}(\boldsymbol{\varepsilon}^\mu - \boldsymbol{\varepsilon}^{\mu p})\mathbf{E}(1-D)(\boldsymbol{\varepsilon}^\mu - \boldsymbol{\varepsilon}^{\mu p})$$

with $\mathbf{E}$ the standard elasticity tensor, which is indeed valid under the assumption of small deformations. Its expression is affected by the damage variable through the effective stress concept introduced above in conjunction with the principle of strain equivalence (Lemaitre and Chaboche, 1990). The plastic energy is assumed as

$$\rho\phi_p^\mu(\boldsymbol{\alpha}^\mu) = \tfrac{1}{3}\mathrm{C}\boldsymbol{\alpha}^\mu : \boldsymbol{\alpha}^\mu$$

with $\boldsymbol{\alpha}^\mu$ the kinematic hardening variable and C the plastic modulus measured on the mesoscale. Note that, accounting for the kinematic hardening, allows to capture the so-called Bauschinger effect, an important phenomenon in fatigue of metals.

As it can be seen, the damage of the material is taken into account via degradation of the elasticity tensor at the microscale. In other words, only the elastic part of the specific free energy at the microscale is affected by the damage variable, thus implying no coupling between hardening and damage.

The thermodynamic (conjugate) forces defined at the microscale are obtained through the following state laws:

$$\boldsymbol{\sigma}^\mu = \rho\frac{\partial\phi^\mu}{\partial\boldsymbol{\varepsilon}^{\mu e}} = \mathbf{E}(1-D) : \boldsymbol{\varepsilon}^{\mu e} \tag{1a}$$

$$\mathbf{X}^\mu = \rho\frac{\partial\phi^\mu}{\partial\boldsymbol{\alpha}^\mu} = \frac{2}{3}\mathrm{C}\boldsymbol{\alpha}^\mu \tag{1b}$$

$$\mathrm{Y}^\mu = -\rho\frac{\partial\phi^\mu}{\partial D} = \frac{1}{2}\boldsymbol{\varepsilon}^{\mu e} : \mathbf{E} : \boldsymbol{\varepsilon}^{\mu e} \tag{1c}$$

where $\mathbf{X}^\mu$ represents the back stress tensor, which is related to the state of internal microstress concentration. Eq. (1b) shows that the hardening is considered by means of a linear (Prager) kinematic hardening rule. The variable Y^μ represents the energy density release rate, which can be rewritten as follows (Lemaitre, 1992):

$$\mathrm{Y}^\mu = \frac{\sigma_{eq}^{\mu 2}\mathrm{R}_v^\mu}{2\mathrm{E}(1-D)^2}$$

with

$$\mathrm{R}_v^\mu = \frac{2}{3}(1+\nu) + 3(1-2\nu)\left(\frac{\sigma_H^\mu}{\sigma_{eq}^\mu}\right)^2 \tag{2a}$$

$$\sigma_{eq}^\mu = (\tfrac{3}{2}\boldsymbol{\sigma}^{\mu D} : \boldsymbol{\sigma}^{\mu D})^{1/2} \tag{2b}$$

$$\sigma_H^\mu = \tfrac{1}{3}\,\mathrm{tr}(\boldsymbol{\sigma}^\mu) \tag{2c}$$

$$\boldsymbol{\sigma}^{\mu D} = \boldsymbol{\sigma}^\mu - \sigma_H^\mu I \tag{2d}$$

where R_v^μ is a triaxiality function, σ_{eq}^μ is the von Mises equivalent stress, σ_H^μ is the hydrostatic stress and $\boldsymbol{\sigma}^{\mu D}$ is the stress deviator. Note that, the role of Y^μ in the continuum damage mechanics framework is identical to that represented by the elastic energy release rate for crack growth, usually denoted by G, in the framework of the classical fracture mechanics.

It has been experimentally observed that microdefects increase in tension and close in compression. Due to this asymmetric behavior, which leads to the so-called crack

closure effect, the energy density release rate Y^μ must assume a different form. According to Ladevéze and Lemaitre (1984), Lemaitre et al. (1999), and Lemaitre and Desmorat (2005), this form should include an additional parameter h, ranging between 0 and 1, as follows:

$$Y^\mu = \frac{1+\nu}{2E}\left[\frac{\mathrm{tr}(\langle\boldsymbol{\sigma}^\mu\rangle^+)^2}{(1-D)^2} + h\frac{\mathrm{tr}(\langle\boldsymbol{\sigma}^\mu\rangle^-)^2}{(1-hD)^2}\right] - \frac{\nu}{2E}\left[\frac{\langle\mathrm{tr}(\boldsymbol{\sigma}^\mu)\rangle^2}{(1-D)^2} + \frac{h\langle-\mathrm{tr}(\boldsymbol{\sigma}^\mu)\rangle^2}{(1-hD)^2}\right]$$

where $\langle\boldsymbol{\sigma}^\mu\rangle^+$ and $\langle\boldsymbol{\sigma}^\mu\rangle^-$ stand for the positive and negative parts of the stress tensor $\boldsymbol{\sigma}^\mu$, respectively, which are defined as follows:

$$\langle\boldsymbol{\sigma}^\mu\rangle^+_{ij} = \langle\sigma^\mu_k\rangle q^k_i q^k_j \quad \text{and} \quad \langle\boldsymbol{\sigma}^\mu\rangle^-_{ij} = \sigma^\mu_{ij} - \langle\boldsymbol{\sigma}^\mu\rangle^+_{ij}$$

with $k=1,2,3$, where σ^μ_k represents the eigenvalue k of the stress tensor $\boldsymbol{\sigma}^\mu$ and $\boldsymbol{q}^k$ its corresponding normalized eigenvector. $\langle(\cdot)\rangle$ stands for the positive part of $(\cdot)$, *i.e.*, $\langle x\rangle = x$ if $x>0$ and $\langle x\rangle = 0$ if $x\le 0$.

Taking into account this effect is especially important when dealing with compressive cyclic loadings as they lead to a damage rate which is much smaller in compression than in tension. Considering this effect also allows to model the mean stress effect in fatigue problems. However, only low mean stress effects can be accounted for by means of the crack closure parameter h (Barbier et al., 2008). As it will be seen later on, as cardiovascular stents are subjected to a very high level of mean stresses, further improvements should be carried out over the present model in this aspect.

2.2. *Complementary state laws*

The model relies on the existence of a plastic–damage dissipation potential given by (see Lemaitre, 1992)

$$F^\mu = f^\mu + F^\mu_x + F^\mu_D$$

with

$$f^\mu = \left(\frac{\boldsymbol{\sigma}^\mu}{1-D} - \mathbf{X}^\mu\right)_{eq} - \sigma_f$$

$$F^\mu_x = 0$$

$$F^\mu_D = \frac{S}{(s+1)(1-D)}\left(\frac{-Y^\mu}{S}\right)^{s+1}$$

where f^μ is the yield function, F^μ_x is the potential associated to the kinematic hardening and F^μ_D represents the damage potential. S and s are material parameters, referred to as the damage strength and the damage exponent, respectively. As it can be seen, the distinction between plasticity and damage mechanisms is considered by assuming the existence of two different dissipation potentials, one for each mechanism. Note that, although considering strain hardening, the present model assumes no dissipation due to such effect. It is also worth mentioning that, the asymptotic fatigue limit σ_f is assumed in this model as a constant, regardless of the mean stress at the mesoscale. For low levels of mean stresses it suffices to consider the mean stress effect by means of the crack closure parameter h. However, for high mean stresses, this is not sufficient.

The complementary state laws (also known as evolution laws) for the plastic internal variables are obtained by means of an associated rule as follows:

$$\dot{\boldsymbol{\varepsilon}}^{\mu p} = \dot\lambda^\mu \frac{\partial F^\mu}{\partial \boldsymbol{\sigma}^\mu} = \frac{3}{2}\frac{\tilde{\boldsymbol{\sigma}}^{\mu D} - \mathbf{X}^\mu}{(\tilde{\boldsymbol{\sigma}}^\mu - \mathbf{X}^\mu)_{eq}}\frac{\dot\lambda^\mu}{(1-D)} \tag{4a}$$

$$\dot{\boldsymbol{\alpha}}^\mu = -\dot\lambda^\mu \frac{\partial F^\mu}{\partial \mathbf{X}^\mu} = \dot{\boldsymbol{\varepsilon}}^{\mu p}(1-D) \tag{4b}$$

Noting that the rate form of the cumulated plastic strain is given by

$$\dot p^\mu = (\dot{\boldsymbol{\varepsilon}}^{\mu p} : \dot{\boldsymbol{\varepsilon}}^{\mu p})^{1/2}$$

the following relation can be obtained by means of Eq. (4a):

$$\dot p^\mu = \frac{\dot\lambda^\mu}{(1-D)} \tag{5}$$

Also the damage evolution law is obtained by means of an associated rule as follows:

$$\dot D = -\frac{\partial F^\mu}{\partial Y^\mu}\dot\lambda^\mu = \left(\frac{-Y^\mu}{S}\right)^s \frac{\dot\lambda^\mu}{(1-D)} = \left(\frac{-Y^\mu}{S}\right)^s \dot p^\mu \quad \text{if } p^\mu > p_D \tag{6}$$

with p_D a damage threshold. As it can be seen from this evolution law, damage is governed by plasticity. Once damage is active, only one multiplier is used to take into account both plasticity and damage evolutions. Damage increases only if there is plastic flow. Likewise, for $p^\mu > p_D$, there cannot exist plastic flow without evolution of damage.

To link matrix and inclusion scales, two different localization laws have been employed. One is based on Lin–Taylor's strain compatibility hypothesis (Taylor, 1938), whereas the other follows the analysis of Eshelby (1957). The former has been employed in Lemaitre (1985), Lemaitre and Chaboche (1990), and Lemaitre and Doghri (1994) and states that

$$\boldsymbol{\varepsilon}^\mu = \boldsymbol{\varepsilon}$$

$$\boldsymbol{\sigma}^\mu = \boldsymbol{\sigma}$$

whereas the latter has been considered in Lemaitre et al. (1999) and Lemaitre and Desmorat (2005) and states that

$$\boldsymbol{\varepsilon}^\mu = \boldsymbol{\varepsilon} + \beta(\boldsymbol{\varepsilon}^{\mu p} - \boldsymbol{\varepsilon}^p) \tag{8a}$$

$$\boldsymbol{\sigma}^\mu = \boldsymbol{\sigma} - 2G(1-\beta)(\boldsymbol{\varepsilon}^{\mu p} - \boldsymbol{\varepsilon}^p) \tag{8b}$$

with G the shear modulus and β a material parameter related to Poisson's ratio as follows:

$$\beta = \frac{2}{15}\frac{4-5\nu}{1-\nu}$$

It is worth recalling that, $\boldsymbol{\varepsilon}$ and $\boldsymbol{\sigma}$ represent the strain and stress mesoscopic tensors, respectively. We will only make use of the latter law, since, according to Lemaitre and Doghri (1994), it is more appropriate to modeling the triaxiality effects than the former.

Introducing a new variable $\boldsymbol{m}^\mu$ defined as

$$\boldsymbol{m}^\mu = \frac{3}{2}\frac{\tilde{\boldsymbol{\sigma}}^{\mu D} - \mathbf{X}^{\mu D}}{(\tilde{\boldsymbol{\sigma}}^\mu - \mathbf{X}^\mu)_{eq}}$$

making use of Eq. (5), and after differentiating the localization law (8a), the constitutive equations (4a), (4b) and (6) can be rewritten, respectively, as

$$\dot{\boldsymbol{\varepsilon}}^{\mu e} + (1-\beta)\dot{p}^{\mu}\boldsymbol{m}^{\mu} = \dot{\boldsymbol{\varepsilon}} - \beta\dot{\boldsymbol{\varepsilon}}^{p} \tag{9a}$$

$$\dot{\boldsymbol{\alpha}}^{\mu} = \dot{p}^{\mu}(1-D)\boldsymbol{m}^{\mu} \tag{9b}$$

$$\dot{D} = \left(\frac{Y^{\mu}}{S}\right)^{s}\dot{p}^{\mu} \quad \text{if } p^{\mu} > p_D \tag{9c}$$

2.3. Damage and microcrack initiation

As noted above, during the material degradation process due to fatigue, the accumulated plastic strain variable p^{μ} and the damage variable D are regarded as evolving quantities. In the framework of the present two-scale plasticity–damage model, while the accumulation of plasticity is viewed as the phenomenon which is responsible for the initiation of damage, the accumulation of damage is regarded as to ultimately lead to the formation of microcracks. Therefore, two distinct criteria need to be specified, one to define the initiation of the damage process, whereas the other to define the microcrack initiation. According to Lemaitre (1992), the criteria for damage and microcrack initiations can be stated, respectively, as follows:

$$p^{\mu} = p_D$$

$$D = D_c$$

where p_D represents the damage threshold and D_c stands for the critical damage parameter.

According to Lemaitre et al. (2000), Lemaitre and Desmorat (2005), and Desmorat (2006), a good estimate of the damage threshold for three-dimensional cyclic loadings is given by

$$p_D = \varepsilon_D^p\left(\frac{\sigma_u - \sigma_f}{\sigma_{eq_{max}} - \sigma_f}\right)^m$$

with σ_u the ultimate stress, ε_D^p the damage threshold in pure tension, and m a correction parameter.

The damage parameter corresponding to microcrack initiation D_c is related to a certain amount of energy dissipated in the damaging process (Lemaitre, 1992; Lemaitre and Doghri, 1994). Assuming a proportional loading (in which R_v^{μ} is constant), the energy dissipated due to damage is given by

$$\int_0^{D_c} Y^{\mu} dD = \int_0^{D_c} \frac{\sigma_f^2 R_v^{\mu}}{2E} dD = \frac{\sigma_f^2 R_v^{\mu}}{2E} D_c$$

Equating this energy to the energy dissipated in a uniaxial tension test gives

$$\frac{\sigma_f^2 R_v^{\mu}}{2E} D_c = \frac{\sigma_u^2}{2E} D_{c_1}$$

where D_{c_1} represents the uniaxial critical damage parameter given by

$$D_{c_1} = 1 - \frac{\sigma_R}{\sigma_u} \tag{11}$$

with σ_R the rupture stress. Hence, the critical damage parameter can be estimated by means of the following expression:

$$D_c = \frac{\sigma_u^2}{\sigma_f^2 R_v^{\mu}} D_{c_1} \leq 1 \tag{12}$$

2.4. Locally coupled analysis—numerical scheme

As noted above, in the high-cycle fatigue regime, material damage is highly localized on a scale which is smaller than either the macro or mesoscales of the material. The two-scale plasticity–damage model presented above, based on the hypothesis of a weak and damageable inclusion embedded in a RVE, has been conceived to capture this phenomenon by means of a locally coupled strain-driven analysis (Lemaitre and Doghri, 1994), which basically consists in performing first a global elastic structural analysis, using for instance the finite element method, to compute the stress and strain variables defined at the mesoscale, followed by a time integration of the elasto-plastic–damage constitutive equations to compute the microscopic stress, strain, hardening and damage variables. The time integration is only performed at critical points, as a post-processing scheme using the history of mesoscopic stresses and strains as inputs, *i.e.*, there is no boundary-value problem to be solved at this stage. This corresponds indeed to a separated multi-scale model, as micro and mesocalculations are performed independently. The time integration is performed step by step until a stabilized cycle is reached, after which a jump in cycles is considered to avoid too many steps, see the following section. This post-processing procedure is repeated until the critical damage value D_c is reached at the critical point, indicating microcrack initiation.

Following Lemaitre and Doghri (1994), the critical point is assumed as the point featuring the maximum damage equivalent mesoscopic stress, defined as $\sigma^* = \sigma_{eq} R_v^{1/2}$, with R_v the triaxiality function defined at the mesoscale. As the stent's material behavior is linear elastic during the cyclic loading, this point does not change from cycle to cycle, and thus it is usually sufficient to perform the post-processing scheme at this single point.

The post-processing scheme introduced above can be summarized as follows. Let us depart from the time instant t_n, characterized by mesoscopic data $\boldsymbol{\varepsilon}_n$, $\boldsymbol{\varepsilon}_n^p$ and $\boldsymbol{\sigma}_n$, and microscopic data $\boldsymbol{\varepsilon}_n^{\mu p}$, $\boldsymbol{X}_n^{\mu}$ and D_n. Note that, the plastic strain at the mesoscale $\boldsymbol{\varepsilon}^p$ has been taken as a constant during the cyclic loading. As note above, this is in accordance with the problem under analysis. The microscale variables at time t_{n+1} are evaluated by means of a three step procedure consisting of:

1. *Local elastic prediction* gives a first estimate of $\boldsymbol{\varepsilon}^{\mu}$, $\boldsymbol{\varepsilon}^{\mu e}$ and $\tilde{\boldsymbol{\sigma}}^{\mu}$ at time t_{n+1} assuming elastic behavior with constant plastic strain $\boldsymbol{\varepsilon}^{\mu p} = \boldsymbol{\varepsilon}_n^{\mu p}$, constant kinematic hardening $\boldsymbol{X}^{\mu} = \boldsymbol{X}_n^{\mu}$ and constant damage $D = D_n$, *i.e.*

$$\boldsymbol{\varepsilon}^{\mu} = \boldsymbol{\varepsilon} + \beta(\boldsymbol{\varepsilon}_n^{\mu p} - \boldsymbol{\varepsilon}^p)$$

$$\boldsymbol{\varepsilon}^{\mu e} = \boldsymbol{\varepsilon}^{\mu} - \boldsymbol{\varepsilon}_n^{\mu p}$$

$$\tilde{\boldsymbol{\sigma}}^{\mu} = \boldsymbol{E} : \boldsymbol{\varepsilon}^{\mu e} = \boldsymbol{\sigma} - 2G(1-\beta)(\boldsymbol{\varepsilon}_n^{\mu p} - \boldsymbol{\varepsilon}^p)$$

2. *Yield condition test:* $f^{\mu} \leq 0$: If this condition is verified, then

$$\boldsymbol{\varepsilon}_{n+1}^{\mu} = \boldsymbol{\varepsilon}^{\mu}$$

$$\boldsymbol{\varepsilon}_{n+1}^{\mu e} = \boldsymbol{\varepsilon}^{\mu e}$$

$$\tilde{\boldsymbol{\sigma}}_{n+1}^{\mu} = \tilde{\boldsymbol{\sigma}}^{\mu}$$

otherwise, integration of the constitutive equations should be carried out (see the third step below).

3. *Local plastic correction*: the constitutive equations (9) are integrated in time by means of an implicit Euler scheme, assuming that the damage remains constant over a whole cycle, which gives the following nonlinear system of equations:

$$\Delta\boldsymbol{\varepsilon}^{\mu e}+(1-\beta)\Delta p^{\mu}\boldsymbol{m}^{\mu}_{n+1}-\Delta\boldsymbol{\varepsilon}=\mathbf{0} \tag{15a}$$

$$\Delta\boldsymbol{\alpha}^{\mu}-\Delta p^{\mu}(1-D)\boldsymbol{m}^{\mu}_{n+1}=\mathbf{0} \tag{15b}$$

$$f^{\mu}_{n+1}=(\tilde{\boldsymbol{\sigma}}^{\mu}_{n+1}-\boldsymbol{X}^{\mu}_{n+1})_{eq}-\sigma_f=0 \tag{15c}$$

In order to apply a Newton-like iterative scheme, the linearization of this set of equations is required. To do so, let us first rewrite Eq. (1a) as follows:

$$\tilde{\boldsymbol{\sigma}}^{\mu}=\mathbf{E}:\boldsymbol{\varepsilon}^{\mu e}=\lambda\,\mathrm{tr}(\boldsymbol{\varepsilon}^{\mu e})\mathbf{I}+2\mu\boldsymbol{\varepsilon}^{\mu e}=\lambda\,\mathrm{tr}(\boldsymbol{\varepsilon}^{\mu})\mathbf{I}+2\mu(\boldsymbol{\varepsilon}^{\mu}-\boldsymbol{\varepsilon}^{\mu p})$$

This, in turn, gives the following relation for the time instant t_{n+1}:

$$\tilde{\boldsymbol{\sigma}}^{\mu}_{n+1}=\lambda\,\mathrm{tr}(\boldsymbol{\varepsilon}^{\mu}_{n+1})\mathbf{I}+2\mu(\boldsymbol{\varepsilon}^{\mu}_{n+1}-\boldsymbol{\varepsilon}^{\mu p}_{n+1})=\lambda\,\mathrm{tr}(\boldsymbol{\varepsilon}^{\mu}_{n+1})\mathbf{I}+2\mu(\boldsymbol{\varepsilon}^{\mu}_{n+1}-\boldsymbol{\varepsilon}^{\mu p}_{n}-\Delta\boldsymbol{\varepsilon}^{\mu p})$$

Under the localization law given by (8a), this expression can be rewritten as

$$\begin{aligned}\tilde{\boldsymbol{\sigma}}^{\mu}_{n+1}&=\lambda\,\mathrm{tr}(\boldsymbol{\varepsilon}_{n+1})\mathbf{I}+2\mu(\boldsymbol{\varepsilon}_{n+1}+\beta(\boldsymbol{\varepsilon}^{\mu p}_{n+1}-\boldsymbol{\varepsilon}^{p})-\boldsymbol{\varepsilon}^{\mu p}_{n}-\Delta\boldsymbol{\varepsilon}^{\mu p})\\&=\lambda\,\mathrm{tr}(\boldsymbol{\varepsilon}_{n+1})\mathbf{I}+2\mu(\boldsymbol{\varepsilon}_{n+1}+(\beta-1)(\boldsymbol{\varepsilon}^{\mu p}_{n}+\Delta\boldsymbol{\varepsilon}^{\mu p})-\beta\boldsymbol{\varepsilon}^{p})\end{aligned}$$

In addition, after integrating in time, Eq. (4a) yields

$$\begin{aligned}\tilde{\boldsymbol{\sigma}}^{\mu}_{n+1}&=\lambda\,\mathrm{tr}(\boldsymbol{\varepsilon}_{n+1})\mathbf{I}+2\mu\boldsymbol{\varepsilon}_{n+1}\\&\quad+2\mu(\beta-1)(\boldsymbol{\varepsilon}^{\mu p}_{n}+\boldsymbol{m}^{\mu}_{n+1}\Delta p^{\mu})-2\mu\beta\boldsymbol{\varepsilon}^{p}\end{aligned} \tag{17a}$$

$$\tilde{\boldsymbol{\sigma}}^{\mu}_{n+1}=\mathbf{E}:\boldsymbol{\varepsilon}_{n+1}+2\mu(\beta-1)\boldsymbol{\varepsilon}^{\mu p}_{n}+2\mu(\beta-1)\boldsymbol{m}^{\mu}_{n+1}\Delta p^{\mu}-2\mu\beta\boldsymbol{\varepsilon}^{p} \tag{17b}$$

After integration in time, Eq. (15b) can be rewritten as

$$\boldsymbol{\alpha}^{\mu}_{n+1}-\boldsymbol{\alpha}^{\mu}_{n}-(1-D)\boldsymbol{m}^{\mu}_{n+1}\Delta p^{\mu}=\mathbf{0}$$

This, on insertion of Eq. (1b), and after multiplying the previous equation by $2C/3$ yields

$$\boldsymbol{X}^{\mu}_{n+1}-\boldsymbol{X}^{\mu}_{n}-\frac{2C}{3}(1-D)\boldsymbol{m}^{\mu}_{n+1}\Delta p^{\mu}=\mathbf{0}$$

Finally, subtracting this equation from (17) yields

$$\begin{aligned}&\mathbf{s}^{\mu}_{n+1}-\mathbf{E}:\boldsymbol{\varepsilon}_{n+1}+2\mu(1-\beta)\boldsymbol{\varepsilon}^{\mu p}_{n}+\left(2\mu(1-\beta)+\frac{2C}{3}(1-D)\right)\boldsymbol{m}^{\mu}_{n+1}\Delta p^{\mu}\\&\quad+2\mu\beta\boldsymbol{\varepsilon}^{p}+\boldsymbol{X}^{\mu}_{n}=\mathbf{0}\end{aligned}$$

with

$$\mathbf{s}^{\mu}_{n+1}=\tilde{\boldsymbol{\sigma}}^{\mu}_{n+1}-\boldsymbol{X}^{\mu}_{n+1}$$

The nonlinear system of Eqs. (15) can, therefore, be replaced by the following set of equations:

$$\mathbf{R}_s=\mathbf{s}^{\mu}_{n+1}+\tfrac{2}{3}q\boldsymbol{m}^{\mu}_{n+1}\Delta p^{\mu}-\boldsymbol{E}:\boldsymbol{\varepsilon}_{n+1}+2G\beta\boldsymbol{\varepsilon}^{p}+2G(1-\beta)\boldsymbol{\varepsilon}^{\mu p}_{n}+\boldsymbol{X}^{\mu}_{n}=\mathbf{0}$$

$$R_p=(\mathbf{s}^{\mu}_{n+1})_{eq}-\sigma_f=0$$

with

$$\mathbf{s}^{\mu}=\tilde{\boldsymbol{\sigma}}^{\mu}-\boldsymbol{X}^{\mu}$$

$$q=3G(1-\beta)+C(1-D_n)$$

$$\boldsymbol{m}^{\mu}=\frac{3}{2}\frac{\mathbf{s}^{\mu D}}{s^{\mu}_{eq}}$$

Note that, this is still a nonlinear system of equations. Its linearization gives the system

$$\mathbf{R}_s+\frac{\partial\mathbf{R}_s}{\partial\mathbf{s}^{\mu}}:\mathbf{C}_s+\frac{\partial\mathbf{R}_s}{\partial p^{\mu}}C_p=\mathbf{0}$$

$$R_p+\frac{\partial\mathbf{R}_p}{\partial\mathbf{s}^{\mu}}:\mathbf{C}_s=0$$

which can be solved iteratively using for instance a Newton-type scheme. $\mathbf{R}_s$, R_p and their partial derivatives are taken at time t_{n+1} and iteration q, and $\mathbf{C}_s$ and C_p are the corrections to be applied to each step of the previous iterated solution $\mathbf{s}^{\mu(q)}$ and $p^{\mu(q)}$. The starting solution corresponds to the elastic predictor, *i.e.*, $\mathbf{s}^{\mu(0)}=\tilde{\boldsymbol{\sigma}}^{\mu}_{n}-\boldsymbol{X}^{\mu}_{n}$ and $p^{\mu(0)}=p^{\mu}_{n}$. The solution of this system can be obtained in closed-form as (Lemaitre and Desmorat, 2005)

$$C_p=\frac{R_p-\boldsymbol{m}^{\mu}:\mathbf{R}_s}{q}$$

$$\mathbf{C}_s=\frac{2}{3}(\boldsymbol{m}^{\mu}:\mathbf{R}_s-R_p)\boldsymbol{m}^{\mu}-\frac{\mathbf{R}_s s^{\mu}_{eq}+\frac{2}{3}q\Delta p^{\mu}(\boldsymbol{m}^{\mu}:\mathbf{R}_s)\boldsymbol{m}^{\mu}}{s^{\mu}_{eq}+q\Delta p^{\mu}}$$

Once the convergence is reached, updating is performed.

2.5. *Jump-in-cycles procedure*

As noted in the preceding section, the time integration of the constitutive equations defined at the microscale is performed step by step until a stabilized cycle is reached, after which a jump in cycles is considered to avoid too many steps. In fact, for periodic loadings of fatigue with large number of cycles, the computation step by step in time may become prohibitive. To overcome this, a jump-in-cycles procedure was proposed by Lemaitre and Doghri (1994). It basically consists in, departing from a cycle N_s, characterized by stabilized damage and accumulated plastic strain rates, predict the damage and accumulated plastic strain values after a 'jump' of a large numbers of cycles ΔN. This procedure is indeed based on a step by step linearization of the damage over large cycle increments.

The jump-in-cycles procedure is divided into two different schemes. One is applied before any damage occurs, *i.e.*, for $p^{\mu}\leq p_D$, whereas the other is used after damage initiation, *i.e.*, for $p^{\mu}>p_D$. In the former, once the computations reach a stabilized cycle N_s, characterized by the accumulated plastic strain rate δp^{μ}_s, a jump of ΔN cycles is considered as follows:

$$\Delta N=\frac{\overline{\Delta p^{\mu}}}{\delta p^{\mu}_s}$$

with $\overline{\Delta p^{\mu}}$ a predefined value. According to Lemaitre and Desmorat (2005), considering $\overline{\Delta p^{\mu}}=p_D/50$ is a good compromise between accuracy and time cost. Finally, the accumulated plastic strain is updated as

$$p^{\mu}(N_s+\Delta N)=p(N_s)+\overline{\Delta p^{\mu}}$$

and used afterwards as the initial value for the computation of the first increment of the cycle $N_s+\Delta N+1$. This scheme repeats until $p^{\mu}=p_D$.

For $p^{\mu}>p_D$, a different scheme is considered as follows. As in the previous scheme, once a stabilized cycle N_s, characterized by the accumulated plastic strain rate δp^{μ}_s and damage

rate δD_s, is reached, a jump of ΔN cycles is considered as follows:

$$\Delta N = \min\left(\frac{\overline{\Delta p}^{\mu}}{\delta p_s^{\mu}}\frac{\overline{\Delta D}}{\delta D_s}\right)$$

with $\overline{\Delta D}$ a predefined value and $\overline{\Delta p}^{\mu} = (S/Y_{max})^s\overline{\Delta D}$, with Y_{max} the maximum value of Y over the cycle N_s. According to Lemaitre and Desmorat (2005), considering $\overline{\Delta D} = D_c/50$ is a good compromise between accuracy and time cost. The accumulated plastic strain and damage variables are finally updated as

$$p^{\mu}(N_s + \Delta N) = p(N_s) + \delta p_s^{\mu}\overline{\Delta N}$$

and used afterwards as the initial values for the computation of the first increment of the cycle $N_s + \Delta N + 1$.

3. Application of the two-scale plasticity–damage model to the fatigue life prediction of cardiovascular balloon-expandable stents

Two stent models will be analyzed in this section. We first analyze a *PalmazShatz* type stent, as this is the one for which we have some available fatigue experimental results, indeed required to validate the numerical results provided by the proposed model. Finally, we analyze a *Cypher* stent, one of the most adopted stent designs nowadays.

We note that, as the first main goal of the present study is to propose a fatigue life numerical method for the analysis of balloon-expandable coronary stents, and not an accurate simulation of the stent implant, the adopted modeling procedure does not take into account the actual stent behavior *in vivo*. More realistic simulations should account for patient-specific vessel geometry and anisotropy of the vessel tissue (Mortier et al., 2010). Also regarding this point, although the inclusion of the balloon can provide a more realistic representation of the transient deformation during the deployment (De Beule et al., 2008; Gervaso et al., 2008), the balloon is herein modeled as an expanding cylinder. Further developments of the present work will focus on the impact evaluation of these aspects on the computation of the stent stress state and the related fatigue life assessment.

3.1. *Finite element stent modeling: model geometry, material properties and analysis*

In the unexpanded configuration, the *PalmazShatz* stent is assumed to be a tube with rectangular slots along its length. Its initial length, inner and outer diameters were taken as 16 mm, 1 mm and 1.2 mm, respectively (strut thickness is 200 μm). The stent has 5 slots in the longitudinal direction and 12 slots in the circumferential direction, each slot measuring 2.88 mm and 0.24 mm, respectively. This stent geometry was also adopted by Auricchio et al. (2001). Fig. 2 shows the geometry and the finite element mesh adopted in the analysis. The mesh was derived from the CAD geometry constructed using Rhinoceros v. 4.0 Educational (McNeel & associates, Seattle, WA, USA).

As for the *Cypher* stent, the length, inner diameter and outer diameter were selected as 8.4 mm, 0.85 mm and 1.15 mm, respectively, *i.e.*, the thickness of the struts were taken as 300 μm. This geometry resembles the *Cypher* stent geometry (Boston Scientific Co., Natick, MA, USA) with a nominal diameter and length of 3 mm and 8 mm, respectively. Fig. 3 represents the geometry and the finite element mesh adopted in the analysis. The adopted finite element mesh was downloaded as an ABAQUS input file from the

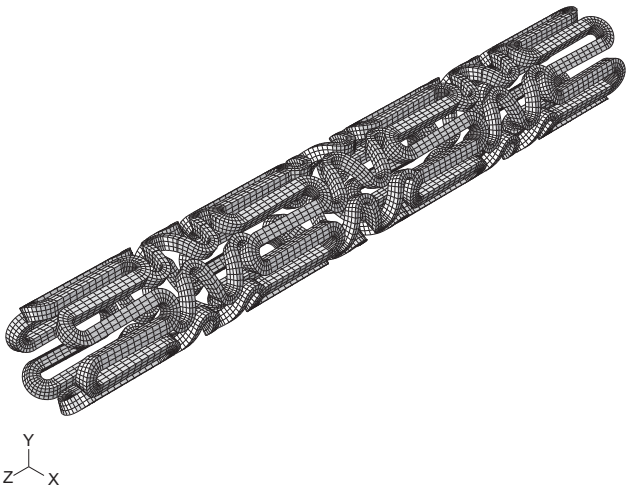

Fig. 3 – *Cypher* stent geometry and finite element mesh.

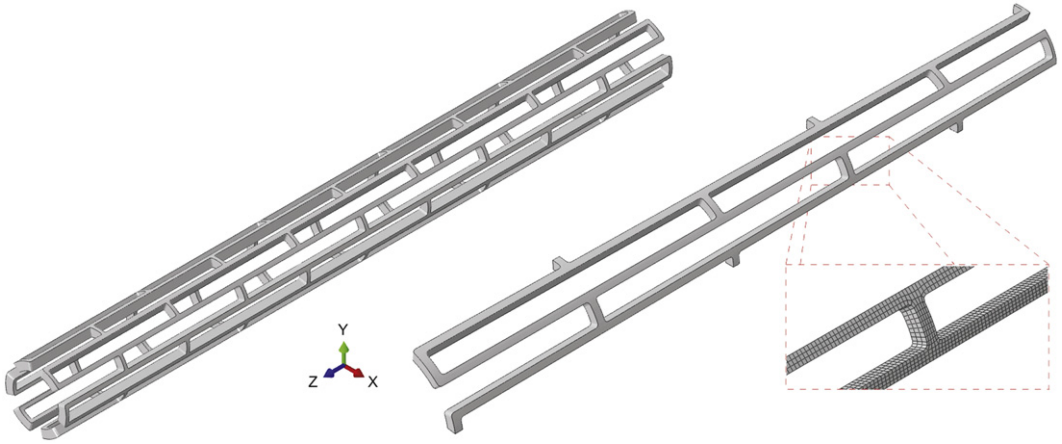

Fig. 2 – *PalmazShatz* stent geometry and finite element mesh.

Ghent University website http://www.stent-ibitech.ugent.be/downloads/downloads.htm.

For both stent designs, the coronary artery was modeled as an idealized vessel represented by a thin-walled pipe with an initial inner diameter of 2.5 mm, wall thickness 0.5 mm and length 12 mm; see Fig. 4.

The *PalmazShatz* stent was assumed to be made of a SS316LN stainless steel, similar to the SS316L steel used in many commercial balloon-expandable stents, such as the original J & J *PalmazSchatz*. As for the *Cypher* stent, it was assumed to be made of a AISI 316L stainless steel. We adopted an elasto-plastic perfect constitutive model for both stent designs, characterized by Young's modulus $E=196$ GPa and Poisson's ratio $\nu=0.3$. As for the yield stress parameter, we adopted $\sigma_y=205$ MPa (see Auricchio et al., 2001) for the *PalmazShatz* stent and $\sigma_y=375$ MPa (see Murphy et al., 2003) for the *Cypher* stent.

The material of the artery wall was modeled using a 5-parameter second-order Mooney–Rivlin hyperelastic model suitable for incompressible isotropic materials. Following Prendergast et al. (2003), Lally et al. (2005, 2006), the strain energy density for this material can be expressed as

$$W=a_{10}(I_1-3)+a_{01}(I_2-3)+a_{20}(I_1-3)^2+a_{11}(I_1-3)(I_2-3)$$

The hyperelastic constants were taken in the present case as $a_{10}=18.9$ KPa, $a_{01}=2.75$ KPa, $a_{20}=85.72$ KPa, $a_{11}=590.43$ KPa.

The analyses of the stents under the mean stress state were performed using the ABAQUS/Standard finite element code (Simulia, Dassault Systems, Providence, RI, USA).

The loadings on the stents were considered in different steps to simulate the loading conditions they experience in service, namely balloon-inflation, recoil, and physiological loading within the artery. For both stent designs, the stent expansion was modeled as a displacement driven process, by enforcing the radial displacements of a rigid cylinder (previously introduced into the stent) to expand the stent to an inner diameter of 3 mm, see Fig. 4. The expansion of the stents was performed into a hyperelastic thin-walled pipe. The hyperelastic tube represents the coronary artery into which the stent is implanted. The stent expansion step was accomplished by modeling contact between the expansion cylinder and the stent, as well as between the stent and the internal surface of the tube. After the expansion step, the stent/vessel systems were allowed to recoil by removing the deployment boundary conditions. This step simulated the balloon deflation and retraction of the balloon catheter. Maximal and minimal uniform pressure loads of 120 mmHg=0.015 MPa and 80 mmHg=0.010 MPa were then sequentially applied to the inner surface of the pipes to conservatively represent physiological systolic and diastolic blood-pressure loads within the arteries. Appropriate boundary conditions were set.

In the *PalmazShatz* stent test case, the stent and the thin-walled pipe were modeled using 10 716 and 6080 C3D8R (8-node three-dimensional brick 'reduced-integration') elements, respectively. The rigid cylinder was modeled using 408 SFM3D4 (4-node quadrilateral surface) elements.

As for the *Cypher* stent case, the stent and the thin-walled pipe were modeled using 31 848 and 15 808 C3D8R (8-node three-dimensional brick 'reduced-integration') elements, respectively, whereas the rigid cylinder was modeled using 1909 SFM3D4 (4-node quadrilateral surface) elements.

The finite element analyses carried out showed that, for the *Cypher* stent test case, although some parts of the stent were characterized by relatively high plastic strains, which is

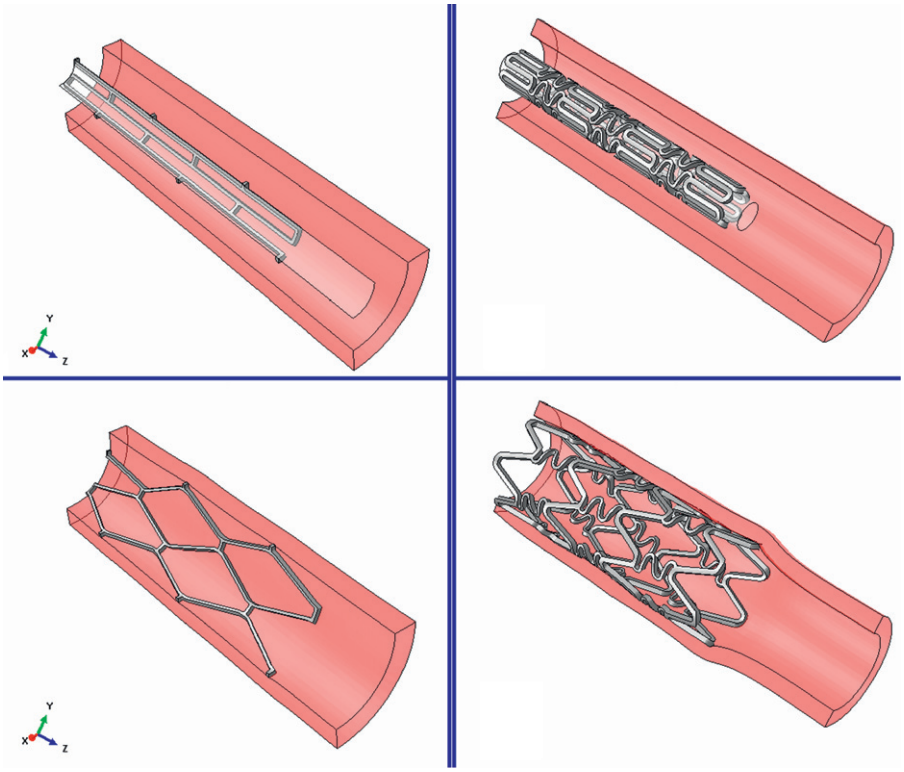

Fig. 4 – View cuts of the stents before and after deployment: left—*PalmazShatz* model and right—*Cypher* model.

indeed a consequence of the expansion and subsequent recoil of the balloon catheter, leading in turn to high residual stresses in the material, the material response was found to be linear elastic during the fatigue cycles. As for the *Palmaz-Shatz* stent case, the material response was found to be elasto-plastic even during the fatigue cycles.

3.2. *Fatigue life assessment methodology*

3.2.1. *Fatigue limit criterion*

Experiments have conclusively shown that, at fixed amplitude the fatigue life decreases as the mean stress increases, see *e.g.* Suresh (1998).

As pointed out recently by Barbier et al. (2008), the crack closure parameter h of the two-scale plasticity–damage model introduced in Section 2 is not sufficient to realistically represent the material behavior at high mean stresses. Hence, as cardiovascular stents work under high level of mean stresses, the model must be modified in the present case. The strategy adopted in this work consists in, rather than using a fixed asymptotic fatigue limit within the yield potential f^{μ}, as suggested by Lemaitre (1985), Lemaitre and Doghri (1994), Lemaitre et al. (1999), Desmorat and Lemaitre (2001), and Lemaitre and Desmorat (2005), taking an asymptotic fatigue limit which varies with respect to the mean stress defined at the mesoscale σ_m. A possible and simple methodology to accomplish this is to use the well known Soderberg (1939) relation given by

$$\sigma_f^m = \sigma_f\left(1-\frac{\sigma_m}{\sigma_y}\right) \tag{22}$$

where σ_f is the asymptotic fatigue limit for zero mean stress and σ_f^m is the new asymptotic fatigue limit taking into account the mean stress effect. In the present context, the mesoscale mean stress can be expressed as

$$\sigma_m = \frac{\boldsymbol{\sigma}_{eq}^{sys} + \boldsymbol{\sigma}_{eq}^{dia}}{2}$$

with $\boldsymbol{\sigma}_{eq}^{sys}$ and $\boldsymbol{\sigma}_{eq}^{dia}$ the systolic and diastolic von Mises equivalent stresses, respectively. It is worth noting that, the Soderberg relation is known in the literature to lead to conservative fatigue predictions. A Goodman relation, where the yield stress σ_y would be replaced by the ultimate stress σ_u in Eq. (22), could alternatively be employed, see *e.g.* Goodman (1899).

3.2.2. *Material parameters identification*

There are nine parameters to be identified: four on the mesoscale (Young's modulus E, Poisson's coefficient ν, yield stress σ_y, asymptotic fatigue limit σ_f and the plastic modulus C), four damage parameters (damage strength S, damage exponent s, damage threshold p_D and critical damage D_c), and the microdefects closure parameter h.

The mesoscale parameters are identified on a monotonic tensile curve. Following Lemaitre et al. (1999) and Lemaitre and Desmorat (2005), the identification of the parameters S, s, p_D, h, D_c can be considered using some fatigue tests, more specifically, an experimental S–N curve and some low-cycle fatigue tests.

It has been shown recently that, the mechanical behavior of cardiovascular stents, which are indeed very small devices with thicknesses of the same order of magnitude as certain microstructural features of the material (such as grains), is size dependent, see *e.g.* Murphy et al. (2003), Wiersma et al. (2006), and Harewood and McHugh (2007).

In order to take into account the size effect, some of the mechanical parameters of the stents, namely, σ_y, σ_u, σ_R and ε_D^p, were explicitly identified from the tensile stress–strain curve obtained by Harewood and McHugh (2007) for a stent of 100 μm of thickness, see Fig. 5. Note that, although the stents under study are 200 μm and 300 μm of thickness, a simple analysis of Fig. 5 indicates that the material parameters for the fatigue model can be identified in a conservative way by selecting the thickness case of 100 μm. Such parameters were identified as $\sigma_y = 375$ MPa, $\sigma_u = 820$ MPa, $\sigma_R = 650$ MPa and $\varepsilon_D^p = 0.28$.

The asymptotic fatigue limit σ_f, defined as the stress at which the fatigue life is 10^7 loading cycles, was identified from the experimental (fully reversed) S–N tests conducted by Agarwal et al. (2007) on a non-treated (NT) stainless steel 316L, see Fig. 6. The arrows indicate run-outs at 10^7 cycles.

The uniaxial critical damage parameter D_{c_1} was computed using formula (11), which gives $D_{c_1} = 0.21$. Following Lemaitre (1992), the triaxiality factor was taken as $R_v^{\mu} = 1$. This is in close agreement with the numerical results obtained for the stents during the fatigue cycles. Eq. (12) gives the critical damage

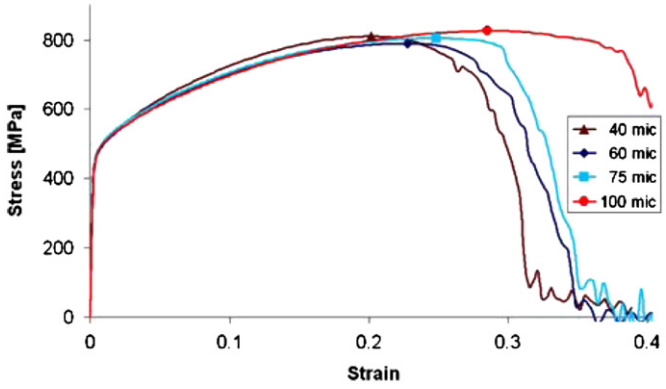

Fig. 5 – Tensile stress–strain curves (taken from Harewood and McHugh, 2007).

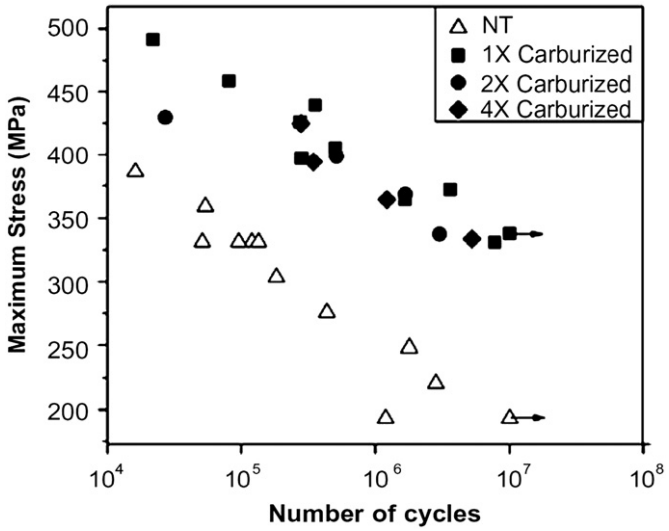

Fig. 6 – Experimental S–N results (taken from Agarwal et al., 2007).

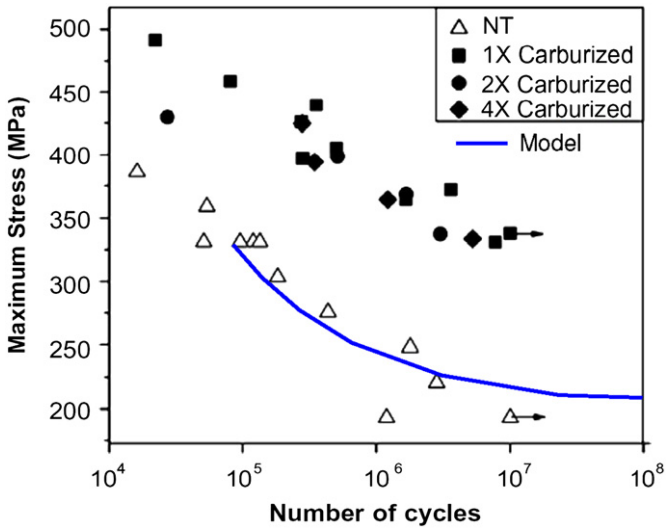

Fig. 7 – Fitting the two-scale model to the experimental S–N results.

Table 1 – Material parameters.

ν	E (MPa)	σ_y (MPa)	σ_u (MPa)	σ_R	ε_{pD}	C (MPa)	D_c	h	σ_f (MPa)	S (MPa)	s	m
0.3	196 000	375	820	650	0.28	1520	1.0	0.2	200	0.8	0.5	1.2

parameter as $D_c=3.4$. However, as the critical damage parameter must verify the condition $D_c \leq 1$, we set $D_c=1$.

Additionally, following Lemaitre and Desmorat (2005), the plastic modulus C was obtained as

$$C = \frac{\sigma_u - \sigma_y}{\varepsilon_D^p} = 1520 \text{ MPa}$$

The crack closure parameter h was set to 0.2. According to Lemaitre (1992), this value allows to obtain numerical results that are in close agreement with fatigue experiments.

There remain three parameters to be identified, namely, s, S and m. These parameters were calibrated using also the experimental S–N results obtained by Agarwal et al. (2007), see Fig. 6. It is worth mentioning that, only the results obtained in the high-cycle fatigue regime (*i.e.*, corresponding to $N>10^5$) were employed for this calibration. This led to the following numerical values: $s=0.5$, $S=0.8$ and $m=1.2$. The numerical S–N curve obtained using the two-scale model is depicted in Fig. 7. As can be seen, it fits well the experimental results in the high-cycle fatigue regime.

The obtained material parameters required for the fatigue analysis were summarized in Table 1.

The initial values of the accumulated plastic strain p^μ and damage D variables were both set to 0.

3.2.3. *Prediction of microcrack initiation*

The critical points of the stents were identified as the Gauss points in which the damage equivalent mesoscopic stress σ^* was maximum. As for the *Cypher* stent model, the material behavior was found to be linear elastic during the cyclic loading. As a result, the critical point does not change from cycle to cycle, and thus it is sufficient to perform the post-processing scheme at this single point. Regarding the *Palmaz-Shatz* stent model, the material response was found to be elasto-plastic during the cyclic loading. For this reason, the post-processing scheme was applied over all the Gauss points of the stent finite element model. The critical point was selected as the one for which the damage variable D first reached the critical damage parameter D_c. The location of the critical point in the *PalmazShatz* stent model can be seen in Fig. 8.

Fig. 9 shows the localization of the critical point in the *Cypher* stent model. Its corresponding stresses and plastic strains were computed for both systolic and diastolic pressure states. Due to the linear elastic response of the stent during cyclic loading, the systolic and diastolic stresses remained unchanged from cycle to cycle, and the plastic strains remained constant during fatigue loading.

The obtained systolic and diastolic stress states at the critical point are

$$\boldsymbol{\sigma}^{sys} = \begin{bmatrix} -350.1 & -82.9 & -22.6 \\ -82.9 & 19.5 & -7.8 \\ -22.6 & -7.8 & -39.8 \end{bmatrix} \text{(MPa)}$$

$$\boldsymbol{\sigma}^{dia} = \begin{bmatrix} -350.2 & -83.3 & -23.2 \\ -83.3 & 19.3 & -8.3 \\ -23.2 & -8.3 & -41.4 \end{bmatrix} \text{(MPa)}$$

Their corresponding von-Mises equivalent stresses are given by $\sigma_{eq}^{sys} = 374.9$ MPa and $\sigma_{eq}^{dia} = 374.7$ MPa. This corresponds to a (very small indeed) stress amplitude of $\Delta\sigma_{eq} = 0.2$ Mpa. The

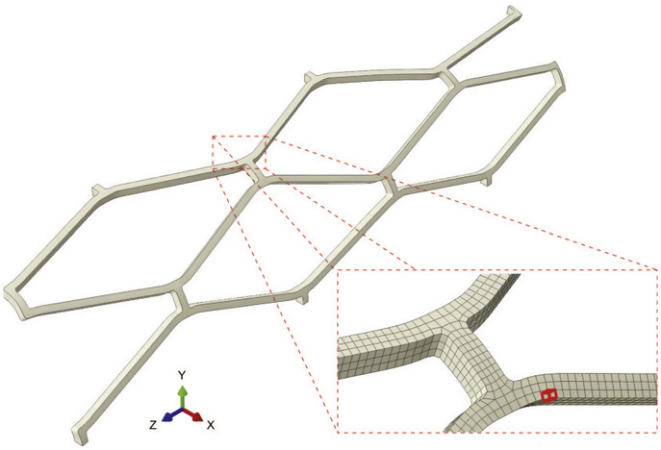

Fig. 8 – Location of the critical point in the *PalmazShatz* stent model.

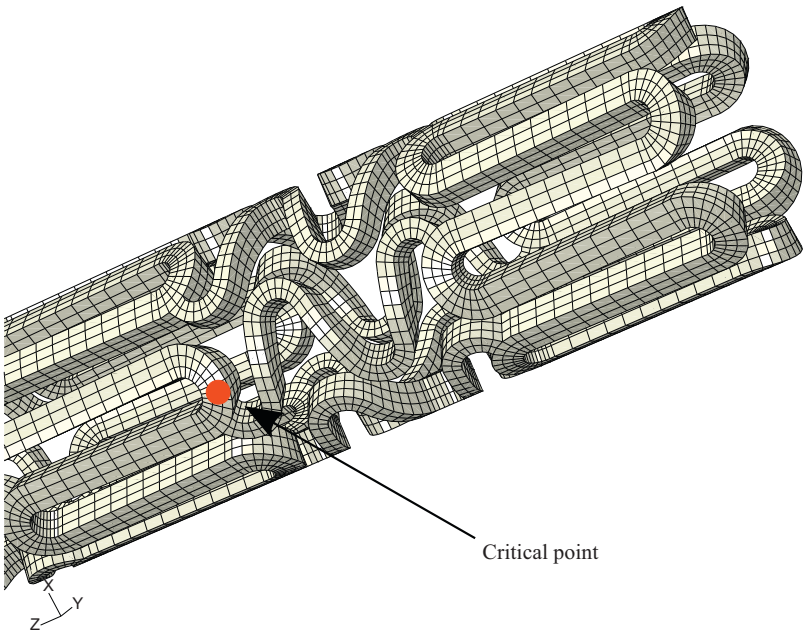

Fig. 9 – Location of the critical point in the *Cypher* stent model.

plastic strains were found to be

$$\varepsilon_{pl} = \begin{bmatrix} -1.33 & 0.04 & 1.21 \\ 0.04 & 0.26 & 0.94 \\ 1.21 & 0.94 & 1.07 \end{bmatrix} \times 10^{-3}$$

Application of the post-processing scheme based on the locally coupled analysis to modeling the stents under the alternating stress states leads to a number of cycles up to microcrack initiation of 64 millions for the *PalmazShatz* stent model, and 53 millions for the *Cypher* stent model. This is equivalent to approximately 22 and 18 months of the heart pumping in an average human adult, respectively.

Although the obtained results correspond to very short fatigue lives, our prediction for the *PalmazShatz* stent design seems to be in accordance with the experiments carried out by Glenn and Lee (1997), in which real stainless steel PalmazShatz™ stents (15 mm long stents from Johnson and Johnson Corporation) were tested to fatigue in a saline solution at 37 °C to simulate real (*in vivo*) physiological conditions. In that work, the criterion for fatigue failure was considered as the rupture of the first strut of the stent. The results obtained by Glenn and Lee (1997) show that, although 2 out of 2 tested stainless steel stents have survived to 1 million cyclic loadings, 0 out of 2 stents have survived to 10 million cycles, only 1 out of 2 stents have survived to 40 million cycles. The experimental results also indicate that 0 out of 4 stents have survived to 100 million cycles.

Clearly, the stent designs under analysis would not satisfy the requirements imposed by the US Food and Drug Administration (FDA), which recommends that a cardiovascular stent must be able to withstand at least 400 million cardiac cycles (equivalent of approximately 10 years) without exhibiting fatigue-associated failure. It is worth mentioning however that the proposed fatigue life assessment method was designed to predict crack initiation, and not fatigue rupture. To predict the total life of the stents up to final failure, the analyses should also take into account the crack propagation effects and proceed with the fatigue analysis using, for instance, a fracture mechanics approach up to final failure. Despite this, we remind that, in the high-cycle fatigue regime, the crack initiation stages may cover a large percentage of the fatigue life and, thus, we would not expect the total fatigue lives of the stent models under analysis to be considerably higher than the ones we obtained.

4. Limitations of the proposed method and future research directions

Relying on a numerical model based inevitably on various hypotheses and simplifications, the proposed method has still certain limitations which may need to be addressed. These limitations, as well as some possible research directions for the development of numerical approaches for the fatigue life assessment of cardiovascular balloon-expandable stents are briefly discussed in the following.

The stent expansion was herein modeled as a displacement driven process, by enforcing the radial displacements of a rigid cylinder. We thus neglected the impact of balloon unfolding and inflation during the deployment. A more realistic simulation should include the (folded) balloon to capture the transient deformation during the deployment (De Beule et al., 2008; Gervaso et al., 2008), and its impact in the final stent tensional state. Further studies should also account for patient-specific vessel geometry and anisotropy of the vessel tissue (Mortier et al., 2010). We believe, however, that these assumptions have a minor role in the present study.

As for the loading conditions, future studies should consider that systolic–diastolic pulsatile pressure is not the only clinical force/deformation mode that must be addressed in bench testing or analysis. Other cyclic deformation modes, such as arterial bending, crushing, axial tension or compression, and torsion can occur, at various frequencies and phases, appearing due to the different physiological forcing functions (*e.g.*, cardiac, respiratory, locomotion), as well as physiological environment, in particular humidity and corrosion conditions, should also be accounted for.

Regarding fatigue life modeling and assessment, it is worth noting that cyclic fatigue characteristics are known to be different for small structures. Hence, experimental fatigue data evaluated for real stents should be employed, rather than well-established bulk material fatigue data. These data are still lacking in the literature, mainly because material forms, such as thin-walled tubing, sheets, or fine wires, are not suitable for the traditional fully reversed strain or stress-cyclic testing. Additionally, the use of more accurate data for the mechanical response of the stent material behavior could be exploited to calibrate the elasto-plastic model hardening.

Finally, at failure locations in stents there are high stress gradients due to stress concentration effects and the small sizes. Stress gradient effects may indeed affect fatigue life. It is well known in the fatigue literature that small stress concentration features or geometries with high stress gradients are less effective in fatigue than larger features or smaller gradients with the same maximum stress (Schijve, 2009). However, it is worth mentioning that only a few fatigue limit criteria currently available in the literature have aimed at modeling such effects, see *e.g.* the work by Morel and Palin-Luc (2002), which shows how far from being well understood the stress gradient effect is still nowadays.

5. Conclusions

A numerical fatigue life approach was presented for the analysis of cardiovascular balloon-expandable (stainless steel) stents. The approach is based on a two-scale continuum damage mechanics model in which both plasticity and damage mechanisms are assumed to take place at a scale smaller than the scale of the representative volume element. The so-called Soderberg fatigue failure criterion was employed within the framework of the two-scale model in order to take into account the high mean stress effects inherent to cardiovascular stents.

The proposed method was applied to the fatigue life assessment of two different stainless steel stent designs, namely, *PalmazShatz* and *Cypher* designs. In both stent models, the obtained results indicate a limited fatigue life. In particular, the results obtained for the *PalmazShatz* stent

model were shown to be in close agreement with the experimental results presented by Glenn and Lee (1997).

The limitations of the proposed method were highlighted, and possible research directions for the development of numerical approaches for the fatigue life assessment of cardiovascular balloon-expandable stents were briefly discussed. We believe that the present methodology can be used to modify the design and prevent failure without testing numerous physical devices, thus preventing from undesired fatigue failures.

Acknowledgments

H.A.F.A. Santos gratefully acknowledges the financial support of the Fundação para a Ciência e a Tecnologia of Portugal under the Post-Doc Grant no. SFRH/BPD/33950/2009. F. Auricchio and M. Conti acknowledge the financial support of the Cariplo Foundation through the Project no. 2009.2822 and ERC Starting Grant through the Project ISOBIO: Isogeometric Methods for Biomechanics (no. 259229). The authors would like also to acknowledge Eng. G. Scalet from the University of Bologna, Italy.

REFERENCES

Agarwal, N., Kahn, H., Avishai, A., Michal, G., Ernst, F., Heuer, A.H., 2007. Enhanced fatigue resistance in 316l austenitic stainless steel due to low-temperature paraequilibrium carburization. Acta Materialia 55, 5572–5580.

AHA., 2010. Circulation 121, e46–e215.

Arakere, A., Grujicic, M., Pandurangan, B., Snipes, J.S., 2012. Fatigue-life computational analysis for the self-expanding endovascular nitinol stents. Journal of Materials Engineering and Performance, http://dxdoi.org/10.1007/s11665-012-0150-2.

Auricchio, F., Di Loreto, M., Sacco, E., 2001. Finite element analysis of a stenotic artery revascularization through stent insertion. Computer Methods in Biomechanics and Biomedical Engineering 4 (3), 249–263.

Aziz, S., Morris, J.L., Perry, R.A., Stables, R.H., 2007. Stent expansion: a combination of delivery balloon underexpansion and acute stent recoil reduces predicted stent diameter irrespective of reference vessel size. Heart 93, 1562–1566.

Barbier, G., Desmorat, R., Sermage, J.-P., du Tertre, A., Courtin, S., Dehouve, J., Tchou-Kien, D., 2008. Mean stress effect by incremental two scale damage model. In: LCF6—6th International Conference on Low Cycle Fatigue, Berlin, Germany.

De Beule, M., Mortier, P., Carlier, S., Verhegghe, B., Van Impe, R., Verdonck, P., 2008. Realistic finite element-based stent design: the impact of balloon folding. Journal of Biomechanics 41, 383–389.

Chaboche, J., 1988a. Continuum damage mechanics: part I—general concepts. ASME Journal of Applied Mechanics 55 (1), 59–64.

Chaboche, J., 1988b. Continuum damage mechanics: part II—damage growth, crack initiation, and crack growth. ASME Journal of Applied Mechanics 55 (1), 65–72.

Desmorat, R., 2006. Damage and fatigue: continuum damage mechanics modelling for fatigue of materials and structures. Geomechanics in Energy Production REGC-10/2006, 849–877.

Desmorat, R., Lemaitre, J., 2001. Continuous damage: a two-scale model for quasi-brittle and fatigue damage. In: Handbook of Materials Behavior Models, Deformations of Materials, vol. 1. Academic Press, pp. 525–535.

Desmorat, R., Kanea, A., Seyedi, M., Sermageb, J.P., 2007. Two scale damage model and related numerical issues for thermo-mechanical high cycle fatigue. European Journal of Mechanics A/Solids 26, 909–935.

Eshelby, J.D., 1957. The determination of the elastic field of an ellipsoidal inclusion and related problems. Proceedings of the Royal Society London A241, 376–396.

Flaceliere, L., Morel, F., Dragon, A., 2007a. Coupling between mesoplasticity and damage in high-cycle fatigue. International Journal of Damage Mechanics 16, 473–509.

Flaceliere, L., Morel, F., Dragon, A., 2007b. Competition between mesoplasticity and damage under HCF—elasticity/damage shakedown concept. International Journal of Fatigue 29, 2281–2297.

Gervaso, F., Capelli, C., Petrini, L., Lattanzio, S., Di Virgilio, L., Migliavacca, F., 2008. On the effects of different strategies in modelling balloon-expandable stenting by means of finite element method. Journal of Biomechanics 41, 1206–1212.

Glenn, R., Lee, J., 1997. Accelerated pulsite fatigue testing of Ni–Ti coronary stents. In: Pelton, A., Hodgson, D., Russell, S., Duerig, T. (Eds.), SMST-97: Proceedings of the Second International Conference on Shape Memory and Superelastic Technologies. SMST Society, Pacific Grove, California, CA, USA.

Goodman, J., 1899. Mechanics Applied to Engineering. Longmans, Green & co., London.

Harewood, F.J., McHugh, P.E., 2007. Modeling of size dependent failure in cardiovascular stent struts under tension and bending. Annals of Biomedical Engineering 35 (9), 1539–1553.

James, B.A., Sire, R.A., 2010. Fatigue-life assessment and validation techniques for metallic vascular implants. Biomaterials 31, 181–186.

Ju, F., Xia, Z., Sasaki, K., 2008. On the finite element modelling of balloon-expandable stents. Journal of the Mechanical Behavior of Biomedical Materials 1 (1), 86–95.

Kachanov, L.M., 1958. Time of the rupture process under creep conditions. Izvestiia Akademia Nauk SSSR 8, 26–31.

Ladevéze, P., Lemaitre, J., 1984. Damage effective stress in quasi unilateral conditions. In: The 16th International Congress of Theoretical and Applied Mechanics. Lyngby, Denmark.

Lally, C., Dolan, F., Prendergast, P.J., 2005. Cardiovascular stent design and vessel stresses: a finite element analysis. Journal of Biomechanics 38, 1574–1581.

Lally, C., Dolan, F., Prendergast, P.J., 2006. Erratum to: "Cardiovascular stent design and vessel stresses: a finite element analysis". Journal of Biomechanics 39, 1760.

Lemaitre, J., 1985. A continuous damage mechanics model for ductile fracture. Journal of Engineering Materials and Technology 107, 83–89.

Lemaitre, J., 1992. A Course on Damage Mechanics. Springer-Verlag, New York.

Lemaitre, J., Chaboche, J.L., 1990. Mechanics of Solid Materials. Cambridge University Press, New York.

Lemaitre, J., Desmorat, R., 2005. Engineering Damage Mechanics: Ductile, Creep, Fatigue and Brittle Failures. Springer Verlag, New York.

Lemaitre, J., Doghri, I., 1994. Damage 90: a post processor for crack initiation. Computer Methods in Applied Mechanics and Engineering 115, 197–232.

Lemaitre, J., Sermage, J.P., Desmorat, R., 1999. A two scale damage concept applied to fatigue. International Journal of Fracture 97, 67–81.

Lemaitre, J., Desmorat, R., Sauzay, M., 2000. Anisotropic damage law of evolution. European Journal of Mechanics—A/Solids 19 (2), 187–208.

Li, J., Luo, Q., Xie, Z., Li, Y., Zeng, Y., 2010. Fatigue life analysis and experimental verification of coronary stent. Heart Vessels 25, 333–337.

Marrey, R.V., Burgermeister, R., Grishaber, R.B., Ritchie, R.O., 2006. Fatigue and life prediction for cobalt–chromium stents: a fracture mechanics analysis. Biomaterials 27 (9), 1988–2000.

McGarry, J.P., O'Donnell, B.P., McHugh, P.E., McGarry, J.G., 2004. Analysis of the mechanical performance of a cardiovascular

stent design based on micromechanical modelling. Computational Materials Science 31, 421–438.

McGarry, J.P., O'Donnell, B.P., McHugh, P.E., O'Cearbhaill, E., McMeeking, R.M., 2007. Computational examination of the effect of material inhomogeneity on the necking of stent struts under tensile loading. Journal of Applied Mechanics 74, 978–989.

Migliavacca, F., Petrini, L., Colombo, M., Auricchio, F., Pietrabissa, R., 2002. Mechanical behavior of coronary stents investigated through the finite element method. Journal of Biomechanics 35, 803–811.

Morel, F., Palin-Luc, T., 2002. A non-local theory devoted to high cycle multiaxial fatigue. International Journal of Fatigue 25, 649–665.

Mortier, P., Holzapfel, G., De Beule, M., Van Loo, D., Taeymans, Y., Segers, P., Verdonck, P., Verhegghe, B., 2010. A novel simulation strategy for stent insertion and deployment in curved coronary bifurcations: comparison of three drug-eluting stents. Annals of Biomedical Engineering 38 (1), 88–99.

Murphy, B.P., Savage, P., McHugh, P.E., Quinn, D.F., 2003. The stress-strain behavior of coronary stent struts is size dependent. Annals of Biomedical Engineering 31 (6), 686–691.

Oller, S., Salomón, O., Oñate, E., 2005. A continuum mechanics model for mechanical fatigue analysis. Computational Materials Science 32, 175–195.

Ottosen, N.S., Stenstrom, R., Ristinmaa, M., 2008. Continuum approach to high-cycle fatigue modelling. International Journal of Fatigue 30, 996–1006.

Pelton, A.R., Schroeder, V., Mitchell, M.R., Gong, X.-Y., Barney, M., Robertson, S.W., 2008. Fatigue and durability of nitinol stents. Journal of the Mechanical Behavior of Biomedical Materials 1 (2), 153–164.

Perry, M., Oktay, S., Muskivitch, J.C., 2002. Finite element analysis and fatigue of stents. Minimally Invasive Therapy & Allied Technologies 11 (4), 165–171.

Prendergast, P.J., Lally, C., Daly, S., Reid, A.J., Lee, T.C., Quinn, D., Dolan, F., 2003. Analysis of prolapse in cardiovascular stents: a constitutive equation for vascular tissue and finite element modelling. ASME Journal of Biomechanical Engineering 125, 692–699.

Rabotnov, Y.N., 1969. Creep Problems in Structural Members. North-Holland Pub. Co, Amsterdam.

Savage, P., O'Donnell, B.P., McHugh, P.E., Murphy, B.P., Quinn, D.F., 2004. Coronary stent strut size dependent stress–strain response investigated using micromechanical finite element models. Annals of Biomedical Engineering 32, 202–211.

Schijve, J., 2009. Fatigue of Structures and Materials. Springer, Netherlands, Amsterdam.

Soderberg, C.R., 1939. Factor of safety and working stress. Transactions of the American Society of Mechanical Engineers 52, 13–28.

Suresh, S., 1998. Fatigue of Materials. Cambridge University Press, New York.

Taylor, G.I., 1938. Plastic strain in metals. Journal Institute of Metals, 62–207.

Wang, W.Q., Liang, D.K., Yang, D.Z., Qi, M., 2006. Analysis of the transient expansion behaviour and design optimization of coronary stents by finite element method. Journal of Biomechanics 39 (1), 21–32.

Weiss, S., Szymczak, H., MeiÔner, A., 2009. Fatigue and endurance of coronary stents. Materialwissenschaft und Werkstofftechnik 40, 61–64.

Wiersma, S., Dolan, F., Taylor, D., 2006. Fatigue and fracture in materials used for micro-scale biomedical components. Bio-Medical Materials and Engineering 16 (2), 137–146.

You, X., Connolley, T., McHugh, P.E., Cuddy, H., Motz, C., 2006. A combined experimental and computational study of deformation in grains of biomedical grade 316lvm stainless steel. Acta Materialia 54, 4825–4840.